Journal of Catalysis 391 (2020) 327–335

Contents lists available at ScienceDirect

Journal of Catalysis

journal homepage: www.elsevier.com/locate/jcat

Electro-oxidation of furfural on gold is limited by furoate self-assembly

Alex M. Román [a,b], Naveen Agrawal [c], Joseph C. Hasse [a,b], Michael J. Janik [c], J. Will Medlin [a,b], Adam Holewinski [a,b,*]

[a] *Department of Chemical and Biological Engineering, University of Colorado, Boulder, CO 80303, United States*
[b] *Renewable and Sustainable Energy Institute, University of Colorado, Boulder, CO 80303, United States*
[c] *Pennsylvania State University, Department of Chemical Engineering, University Park, PA 16802, United States*

ARTICLE INFO

Article history:
Received 23 June 2020
Revised 16 August 2020
Accepted 18 August 2020
Available online 7 September 2020

Keywords:
Furfural
Furoic acid
Electrochemical oxidation
Electrolysis flow cell
ATR-SEIRAS

ABSTRACT

Processing of biomass-derived compounds with electrocatalysis has shown promise to directly couple the production of valuable feedstocks with the storage of renewably produced electricity. One potential route of electrocatalytic conversion is the partial oxidation of furfural to furoic acid (FA), a precursor to 2,5-furandicarboxylic acid (FDCA). We have utilized differential electrochemical reactor studies along with infrared spectroscopy (ATR-SEIRAS) experiments and density functional theory (DFT) calculations to probe the oxidative reaction pathways of furfural on gold catalysts in acidic electrolyte. We find furfural electro-oxidation activity (~2 $\mu A/cm^2_{Au}$ at 1.0 V_{RHE}) to be an order of magnitude higher than that observed on Pt/C. 96 ± 6% Faradaic efficiency to FA is achieved at 0.8 V_{RHE}. Product desorption is rate limiting, and spectroscopic evidence indicates that the most abundant intermediate is surface furoate. Deeper oxidation products observed with dilution of furfural suggest that self-assembly of the furoate species contributes to selectivity.

1. Introduction

Furoic acid (FA) has recently gained attention as an alternative biomass-derived precursor to 2,5-furan-dicarboxylic acid (FDCA), a promising bio-renewable monomer produced mainly from 5-(hydroxymethyl)furfural (HMF) [1–5]. FA, which is commonly used as a preservative, fungicide, and pharmaceutical precursor, can be derived from furfural, a product of the acid-catalyzed hydrolysis of hemicellulose sources such as sugar cane [6]. The conventional methods for FA production require either the addition of a strong base (e.g. NaOH) to disproportionate furfural into both FA and furfuryl alcohol (Cannizarro reaction) [7] or the addition of a chemical oxidizer (e.g. O_2, H_2O_2), typically in the presence of a catalyst and at elevated temperature and pressure [8–11]. Electrochemical methods offer a unique opportunity to convert furfural directly to FA without the need to alkalize the acidic aqueous feedstock, provide an oxidizing agent, or perform costly extra separations (Scheme 1) [12]. Electrocatalytic oxidation processes typically operate at lower reaction temperatures and pressures as they are activated via an applied potential—ideally utilizing renewable electricity resources—and are paired with reduction processes that can co-produce H_2 [13–16] and/or fuels [17–20]. Combined with methods of FA carboxylation (a supplemental means of sequestering CO_2), the resulting FDCA monomer has the potential to be carbon neutral [1]. In recent work, we illustrated that the electrocatalytic partial oxidation of furfural to FA in acidic electrolyte is achievable on Pt/C, albeit with moderate selectivity to FA below 1.0 V_{RHE} and low overall activity (<1 $\mu A/cm^2_{Pt}$) [21,22].

Noble metal catalysts generally serve as stable anodes under acidic conditions. Thus, studying partial oxidations on noble metals serves as a beneficial starting point to develop fundamental mechanistic understanding. Furan oxidation catalyzed by supported Au and Au-alloys has been found to be selective and active towards carboxylic acid (FA and FDCA) production, either using O_2 as the oxidant [9,23–25] or via electrochemical oxidation in basic electrolytes [26,27]. The present study investigates the activity and Faradaic efficiency of the electro-oxidation of furfural to FA on Au in acid electrolyte, which is most relevant to real feedstocks generated by biomass hydrolysis or pyrolysis. The side products 5-hydroxy-furan-2(5H)-one (HFN) and maleic acid (MA) were found to be minor products at high overpotential, consistent with previous electrochemical studies on other surfaces in acidic electrolyte (Scheme 1) [28,29]. DFT calculations and experiments using ATR-SEIRAS suggest that FA readily oxidizes to a surface bound furoate species, the desorption of which is found to be rate-limiting and potential-dependent. A proposed mechanism of catalyst deactivation due to the buildup of furoate is discussed.

---

[*] Corresponding author.
E-mail address: adam.holewinski@colorado.edu (A. Holewinski).

https://doi.org/10.1016/j.jcat.2020.08.034

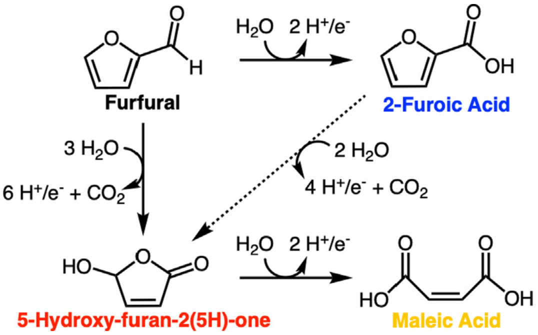

Scheme 1. Furfural electro-oxidation pathways to furoic acid (FA), 5-hydroxy-furan-2(5H)-one (HFN) and maleic acid (MA).

2. Experimental methods

2.1. Materials

All solutions were prepared using ultrapure (UP) deionized water (>18.2 MΩ-cm, Millipore). Furfural (99%, Sigma-Aldrich) was purified by vacuum distillation then stored at −70 °C until used in experiments. All other reagents and standards were used as delivered: Suprapure® perchloric acid (70%, MilliporeSigma), Pt gauze (Alfa Aesar), 2-furoic acid (98%, Sigma-Aldrich), 5-hydroxy-2(5H)-furanone (96%, Enamine LLC), maleic acid (99%, Sigma-Aldrich), 40% Au/C (Ketjenblack support, Premetek, XRD crystallite size = 4–6 nm), ethanol (anhydrous, Decon Labs Inc.), 5% and 20% w/w Nafion solution in aliphatic alcohols (Sigma-Aldrich), argon (UHP, Air-Gas), hydrogen (UHP, AirGas), 2-propanol (HPLC Grade, Sigma-Aldrich), and plain carbon cloth (AvCarb Material Solutions).

2.2. Differential electrolysis flow cell

A custom-built flow-through electrolysis cell was used to assess oxidation catalysts while minimizing impact from secondary products and slow homogeneous chemistries. A detailed description of the flow cell can be found in Ref. [21]. The reference electrode (RE) consisted of a Pt wire (Alfa Aesar) bubbled over with H_2 and isolated via a Nafion junction to create a reversible hydrogen electrode (RHE). All reported potentials are on a RHE scale. The counter electrode (CE) was a Pt wire mesh (Alfa Aesar) with a geometric surface area of ~4 cm^2. Both the CE and RE were flame-polished and quenched in UP water immediately prior to use, and sit downstream of the WE, so no contamination or Pt migration will affect the working electrode (WE). The WE consisted of a Au/C (40 wt%Au) ink deposited on plain carbon cloth. The ink was prepared with 4 mg_{Au} per 1 mL of total ink containing 0.9 mL ethanol, 0.1 mL UP water and 10 μL 5% Nafion ionomer solution. Inks were sonicated for at least 1 h prior to application onto the carbon cloth working electrode (WE).

Electrochemical characterization was performed with a Gamry Reference 3000™ potentiostat. Uncompensated resistance (R_u) was evaluated prior to each experiment and typically fell in the range of 5–15 Ω, as determined from Electrochemical Impedance Spectroscopy (EIS). All currents and potentials are reported with *iR*-correction and versus RHE. In a typical experiment, 100 mL of electrolyte were de-aerated by bubbling argon gas at 60 sccm for 30 min prior to being pulled into a clean 60 mL syringe. The syringe was then quickly connected to the flow cell using PTFE tubing and electrolyte was flowed through the cell using a syringe pump. Flow rate was varied to confirm elimination of mass transfer effects, and 0.05 mL/min was found sufficient under all conditions. A break-in procedure consisted of cycling the catalyst from 0.1 to 1.5 V at 100 mV/s for 50 cycles prior to use. After break-in, freshly de-aerated electrolyte containing 100 mM furfural was introduced to the cell (at 0.05 mL/min) under potential control at 0.6 V to flush the reactor for 20 min prior to experiment. This flow rate resulted in a residence time of ~8 s through the catalyst bed. Product yields and electron balances were used to estimate the conversion, which was below 2% in all experiments.

Chronoamperometry experiments consisted of setting the operating potential for the WE and allowing the reaction to come to steady state over 30 min. The steady state current was recorded as samples were collected over an additional 30 min into Parafilm-covered 1.5 mL micro-centrifuge tubes. Each flow reactor experiment was performed in triplicate. Full calculation details for partial currents, selectivity, and Faradaic efficiencies can be found in the SI. The electrochemical surface area (ECSA) was measured by integrating the reduction peak of Au oxide in the range from 0.95 to 1.3 V using the conversion factor of $300 \mu C/cm^2_{Au}$ [30].

The flow cell was cleaned between experiments by sequential sonication in acetone, 2-propanol, and UP water, 30 min each at 50 °C. The cell was then placed into a H_2SO_4/NoChromix® cleaning bath overnight to remove residual organic species, then boiled in UP water 5 times prior to use.

2.3. In situ infrared spectroscopy

An Au nanoparticle film was chemically deposited on the total reflecting plane of an Irubis Specialized 1 single reflection ATR crystal via an electroless plating method originally developed by Miyake et al. [31]. The wafer was mechanically polished using progressively finer alumina slurries (5 μm, 0.3 μm, 0.05 μm) as polishing agents. The crystal was then placed in a 50:50 mixture of UP water and isopropanol for 20 min, then in UP water for 20 min. The nontextured Si surface was then etched using a 40% NH_4F (Sigma-Aldrich) solution to remove the native oxide layer and terminate the surface with hydrogen. Finally, a room temperature solution of a plating solution, compromised of 0.015 M $NaAuCl_4 \cdot 2 H_2O$ + 0.15 Na_2SO_3 + 0.05 M $Na_2S_2O_3$ + 0.05 M NH_4Cl, was droppered onto the nontextured surface of the crystal at 60 °C for 1 min, then rinsed with DI water. While this surface was not identical to the supported Au/C catalysts, the deposition protocol is well established to generate a polycrystalline film with nanoscale roughness.

The surface-enhanced infrared reflection-absorption spectroscopy (SEIRAS) measurements were taken using a Jackfish J1W Spectroelectrochemical cell mounted to a Pike Veemax III accessory with an incident angle of 35°. Infrared spectra were recorded using *p*-polarized light from a Nicolet 6700 FT-IR Spectrometer (Thermo Electron) equipped with a liquid nitrogen-cooled MCT-A detector. Spectra were acquired at a resolution of 4 cm^{-1}. A "leak-free" Ag/AgCl (Innovated Instruments) reference electrode was used and a platinum wire mesh served as the counter electrode.

2.4. Liquid chromatography

Reaction products were primarily analyzed by an Advion 2000 HPLC equipped with a UV Diode Array Detector (DAD) as well as an Advion Expression Compact Mass Spectrometer – S Series. The mobile phase consisted of Optima® Water (Thermo Scientific) with 0.01% formic acid in isocratic mode at a flow rate of 0.2 mL/min. Undiluted samples collected from the flow cell were filtered through a 0.2 μm hydrophilic PTFE membrane (Millipore) into amber vials. The autosampler temperature was set to 4 °C to minimize degradation of furfural prior to sampling. Aliquots of 100 μL were injected into a 300 mm × 6.5 mm sulfonated polystyrene gel column (Hi-Plex H, Agilent) at 50 °C with eluent diverted for the first 20 min of the method to avoid introduction of the corrosive electrolyte to the ion source. Products were confirmed using Atmospheric Pressure Chemical Ionization (APCI) alternating positive (3 μA) and negative (25 μA) ionization modes. The source gas (N_2) temperature was set to 300 °C and flowed at 4 L/min. The ionized vapor impinged onto a capillary inlet at 200 °C with a capillary voltage of 120 V. Products were confirmed by injection of a known standard. Products were quantified via UV DAD using the following wavelengths: maleic acid (215 nm), 5-hydroxy-2(5H)-furanone (200 nm), and furoic acid (251 nm). External calibration curves were produced from standard solutions made in the working electrolyte.

2.5. Density functional theory methods

DFT calculations were performed within the Vienna Ab initio simulation package (VASP, version 5.3.5), using the periodic supercell approach. The projector augmented wave (PAW) method was used for electron-ion interactions [32,33]. The Perdew-Burke-Ernzerhof exchange-correlation functional [34] was used with dispersion correction (PBE-D3) [35–37] added. We have previously used the PBE-D3 functional to examine furfural oxidation surface chemistry on the Pt(1 1 1) surface, and provided energetic data that supported observed experimental phenomena [22,38]. The plane wave basis set energy cutoff was 450 eV. Structures were converged until atomic forces were less than 0.05 eV Å^{-1}. Transition state structure searches used the climbing image nudged elastic band (CI - NEB) method [39]. Transition state atomic forces met the same 0.05 eV Å^{-1} convergence, and we confirmed all transition state structures have a single imaginary vibration mode along the reaction coordinate.

For isolated molecule calculations, a cubic cell of 15 × 15 × 15 Å^3 was used. The Pt (1 1 1) and Au(1 1 1) metal slabs were constructed with a 3 × 3 unit cell composed of five atomic layers. The bottom three layers were frozen at their bulk lattice positions, with lattice constants 3.976 Å (Pt) and 4.078 Å (Au), determined as optimal with DFT. The vacuum region between the slabs, before adding adsorbates, was 20 Å to avoid interactions between periodic slabs. In this initial mechanistic analysis, we do not consider solvation of surface adsorbed species or the charging of the electrode/electrolyte interface. Spurious slab-to-slab dipole interactions were corrected (VASP keywords LDIPOL = TRUE, IDIPOL = 3).

2.6. Elementary electrochemical reaction energies

The geometries of all surface furfural oxidation intermediates were fully optimized, considering multiple initial adsorption configurations to determine the lowest energy structures. All relative energies presented herein are zero-point vibrational energy (ZPVE) corrected and surface species include a vibrational entropy term. The free energy of an adsorbed intermediate is calculated as:

$$G^*_{int} = E^*_{int} + E_{ZPVE} + E_{vib} - TS_{vib} \tag{1}$$

where E^*_{int} is the DFT optimized energy of the adsorbed intermediate, E_{ZPVE} is the zero-point vibrational energy,E_{vib} is the internal energy stored in vibration at 300 K, and TS_{vib} represents the vibrational entropy of the adsorbed species at 300 K.E_{vib} and TS_{vib} are calculated using standard ab-initio thermodynamic approaches [40].

Free energies of gas phase species are calculated by including PV, translational, rotational, and vibrational energy and entropy terms, treating each species as an ideal gas. The free energy of water was calculated at 0.03 atm, the vapor pressure of water at atmospheric conditions, to match the chemical potential of liquid water at 300 K and 1 atm, whereas all other gas phase chemical potentials are determined at 1 atm.

The free energy of each surface intermediate $C_XH_YO^*_Z$ is calculated relative to gas phase furfural and a bare surface slab using the computational hydrogen electrode (CHE) approach:

$$C_5H_4O_2 + * \rightarrow C_XH_YO^*_Z + (2X - Z - 8)H_2O_{(l)} + (5 - X)CO_{2\,(gas)}$$

$$+(20 + 2Z - 4X - Y)\left(H^+ + e^-\right) \tag{2}$$

Relative energies at a potential (U) on the CHE (or, equivalently, reversible hydrogen electrode, RHE) scale are calculated:

$$\begin{aligned} RE(U) = {} & G_{C_XH_YO^*_Z} - G_{FF} - E_{surf} + \left(\frac{20 + 2Z - 4X - Y}{2}\right)G_{H_2} \\ & + (2X - Z - 8)G_{H_2O(l)} + (5 - X)G_{CO_2(g)} - (20 + 2Z - 4X - Y)eU \end{aligned} \tag{3}$$

$G_{C_XH_YO^*_Z}$ is the ZPVE corrected free energy of the adsorbed intermediate, G_{FF} is the free energy of an isolated furfural molecule, E_{surf} is the energy of the relaxed bare surface, and G_{CO_2}, G_{H_2} and G_{H_2O} are the free energies of gas phase CO_2, H_2 and H_2O, respectively. The value of '**e**' in the final term is the absolute value of the electron charge. Adsorption energies were calculated using Eq. (4):

$$\Delta E_{ads} = E^*_i - E_i - E_{surf} \tag{4}$$

where E_i is the energy of the isolated intermediate, E_{surf} is the energy of the bare surface, and E^*_i is the energy of the intermediate adsorbed on the surface. A negative ΔE_{ads} corresponds to a stable adsorbate–surface system.

2.7. Potential-dependent activation barriers

Activation barriers as a function of electrode potential U were calculated based on the Butler-Volmer formalism as detailed in prior work [41,42]. This method allows us to approximate potential dependent activation barriers by calculating the transition state for the non-electrochemical X-H dissociation or C—OH formation step, then assign the calculated barrier to the potential at which the H or OH species in the unit cell has the same chemical potential of the water, protons, and electrons involved in generating it. The potential dependent activation barrier is determined by:

$$E_{act}(U) = E^0_{act}(U^0) - \beta e\left(U - U^0\right) \tag{5}$$

$E^0_{act}(U^0)$ is the activation barrier calculated for non-electrochemical reactions used as equivalent to the electrochemical step being studied. For deprotonation reactions of the form $(AH)^* \rightarrow A^* + H^+ + e^-$, surface dehydrogenation reactions are used and U^0 is calculated by:

$$U^0 = \frac{G_{A^*} + \frac{1}{2}G_{H^*_2} - G_{(A^*+H^*)}}{e} \tag{6}$$

For reactions of the form $A^* + H_2O \rightarrow (A\text{-}OH)^* + H^+ + e^-$, the non-electrochemical addition of a surface bound OH* species to the co-adsorbed A* species is used to evaluate $E^0_{act}(U^0)$, and U^0 is calculated by:

$$U^0 = \frac{G_{(A^*+OH^*)} + \frac{1}{2}G_{H^*_2} - G_{A^*} - G_{H_2O}}{e} \tag{7}$$

β is a reaction symmetry factor denoting the relationship between the activation barrier and reaction energy change [43]. β is typically between 0.3 and 0.7 [44,45], and we approximate that β is equal to 0.5 for all one electron steps. The barrier is taken to have reached 0 when Eq. (5) produces a negative barrier. The most stable geometries of all the relevant intermediates and transition states are shown in Figs. S8 and S9.

3. Results and discussion

3.1. Voltammetry of furfural on Au

Electrochemical interactions between furfural and Au/C were first assessed as a function of furfural concentration using cyclic voltammetry (CV). The potential was scanned from 0.1 to 1.5 V in 0.25 M $HClO_4$ electrolyte in a standard 3-electrode cell (Fig. 1). The anodic scan showed the onset of a primary oxidation process at ~0.8 V, with a relatively low current density peaking at 0.9 V then gradually subsiding until ~1.2 V where a more pronounced secondary oxidation process began. The total oxidation current at the primary oxidation peak was only weakly sensitive to furfural concentration, with little difference in peak current at concentrations greater than 50 mM (Fig. 1 inset). At potentials greater than the oxidation potential of Au (>1.2 V) the secondary oxidation process showed a similar weak concentration dependence. On the cathodic sweep, the Au reduction peak diminished in magnitude with increasing furfural concentration. This decrease indicates that the presence of furfural or other organic intermediates on the Au surface inhibit oxidation of the Au. Further, the CV currents appear asymptotically sensitive to the concentration of furfural, indicating a saturating effect on the coverage of surface species.

3.2. Steady state electro-oxidation studies

The initial product distribution of furfural oxidation was determined using a differential electrolysis flow reactor with a Au/C packed bed electrode. The potential window of interest was constrained between 0.8 and 1.3 V to further probe contributions to the cyclic voltammetry observations and to limit interference from competitive side reactions at high overpotential (mainly OER and breakdown of the carbon support). Operation in a kinetically-controlled regime was confirmed by flow rate variation. Major products of furfural oxidation consisted of furoic acid (FA) and 5-hydroxy-2(5H)-furanone (HFN), with small amounts of maleic acid produced as well (Fig. 2). In our previous study on Pt/C, HFN, 5-hydroxyfuroic acid (HFA), and 2(3H)-furanone (3FN) were found to be major products at high overpotentials (>1.1 V); however, 3FN and HFA were found to account for little-to-no product yields in the same potential window on Au/C. The partial current and Faradaic efficiency to each major product are reported as a function of applied potential in Fig. 2. FA was the dominant product at all potentials investigated. Partial currents to FA peaked at 1.0 V and were ~10× higher (on ECSA basis) than previously seen on Pt/C under identical conditions [21]. Starting at 1.2 V, the partial current to more oxidized products increased substantially; nearly 50% of the current went to further oxidized products when potential was increased to 1.3 V (~10% is attributed to carbon support breakdown at this voltage, with negligible contributions at other conditions). The lack of significant other liquid-phase products (as determined by LCMS and NMR, more details in SI) suggests complete oxidation to CO_2 as the predominant unspecified product at these potentials. The selectivity toward the over-oxidation to HFN increased at 1.3 V, suggesting that changes in coverage due to faster rates of desorption (discussed further below) and/or onset of an AuO_x surface phase may play a role in activating the decarbonylation of furfural and/or the decarboxylation of the product FA. For comparison, the steady state oxidation of FA as feed (Fig. S1) showed no activity at potentials below 1.0 V, and substantially lower total oxidation currents a partial currents to HFN and MA between 1.0 and 1.3 V. As was the case with furfural oxidation, the amount of unaccounted current rose considerably at 1.3 V and is likely associated with complete oxidation of FA.

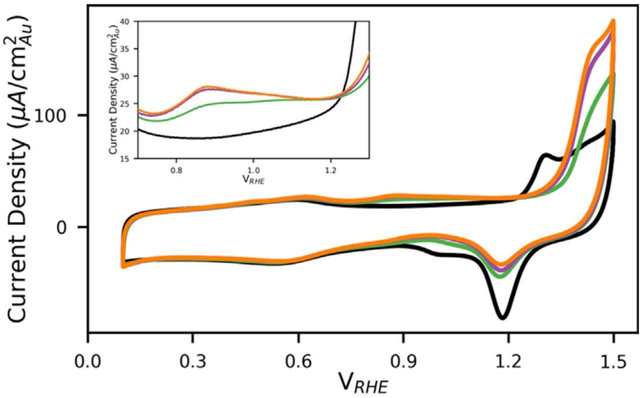

Fig. 1. Cyclic voltammograms for Au/C in 0.25 M $HClO_4$ without (black) and with 10 mM (green), 50 mM (purple), and 100 mM (orange) furfural present. *Inset*: Expanded view of the onset of furfural oxidation starting at 0.8 V. Scan rate = 20 mV/s.

Similar to the voltammetry experiments, varying the initial concentration of furfural had little effect on the total steady-state oxidation current and product distribution at concentrations greater than 50 mM. The partial current density and F.E. to the major products FA and HFN is shown at several feed concentrations of furfural in Fig. 3. At 10 mM the partial current to FA was less than half of that at 50 or 100 mM at any given potential, with similar F.E.'s to FA at potentials below 1.0 V affirming that there were minimal side paths. In contrast, at potentials above 1.0 V, 10 mM furfural showed an increase in HFN production, suggesting that this pathway may be facilitated by decreased furfural surface coverages (induced by the combination of low concentration and rising turnover rate), freeing more sites for the furan ring to directly interact (parallel) with the Au surface. This "flat-lying" conformation has been found as a key intermediate for furfural decarbonylation on other surfaces [46–48]. Transition toward AuO_x may also impact C—C bond breaking at 1.3 V.

The lack of concentration dependence approaching higher concentrations suggests that the rate of furfural oxidation is not limited by the rate of adsorption. If the rate were limited by surface reaction, markers of competition between furfural and oxidative equivalents (presumably adsorbed OH) would be present. While there is perhaps a slight downturn in FA production at the highest concentration point, this is within error. More critically, the amount of adsorbed hydroxide should be expected to respond strongly to potential, and the nearly identical performance spanning from 0.9 to 1.1 V suggests that OH does not effectively compete for surface sites when its chemical potential is increased. Thus the apparent zero-order kinetics with respect to reactants is most suggestive of limitation by product desorption. This finding is consistent with infrared studies presented next.

3.3. ATR-SEIRAS studies

Surface species present during furfural oxidation were probed using in situ ATR-SEIRAS on a polycrystalline Au thin film electrode with nanoscale roughness [31]. Spectra for furfural and FA are shown as a function of potential over a slow CV (5 mV/s) in Fig. 4, scanning from 0.3 to 1.3 V starting at the bottom of the figure. With only FA present (Fig. 4a), peaks centered at 1582, 1477, 1412, and 1373 cm^{-1} were formed beginning at 0.8 V, cresting in intensity at 1.3 V, then returning to baseline by 0.3 V on the return sweep. The peak at 1373 cm^{-1} is attributed to a bidentate, symmetric OCO stretch associated with the upright conformation of furoate binding via a deprotonated carboxylate group; strong peaks in this region are commonly seen for ATR-SEIRAS studies with aromatic acids on Au electrodes and vibrational frequency

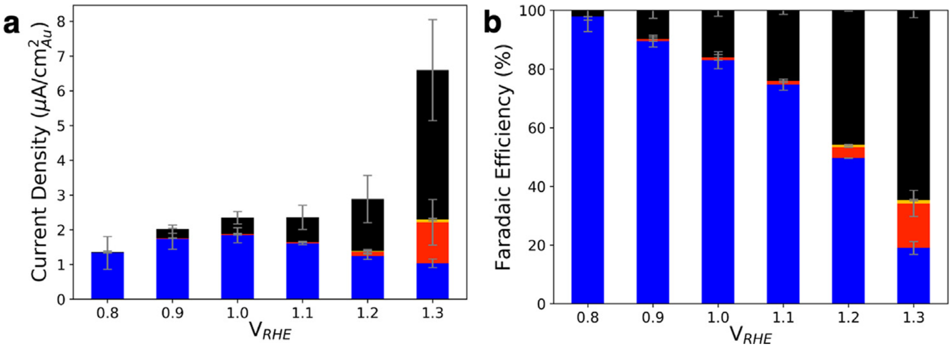

Fig. 2. (a) Partial current density and (b) Faradaic efficiency to FA (blue), HFN (red), MA (yellow), and deeper oxidation products (e.g. CO_2, black) from the steady-state oxidation of 100 mM furfural in 0.25 M $HClO_4$ on Au/C.

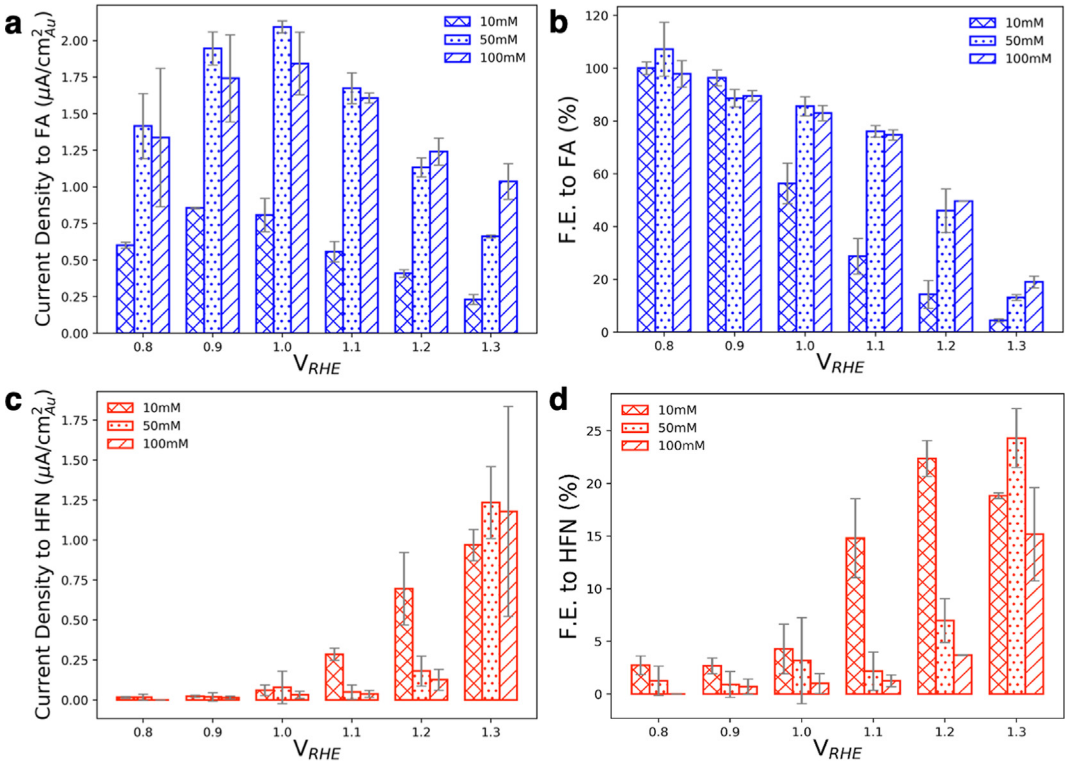

Fig. 3. Effect of furfural concentration on the partial current density and Faradaic efficiency to (a, b) FA and (c, d) HFN from the steady-state oxidation of furfural in 0.25 M $HClO_4$ on Au/C.

DFT calculations have confirmed this is a plausible assignment (Table S1) [49–51]. The remaining peaks at 1582, 1477, and 1412 cm^{-1} have each been assigned to ring stretches of the upright oriented bidentate furoate species based (i) on the lack of evidence for HFN or MA formation (control spectra shown in Figs. S4 and S5, respectively), (ii) agreement with vibrational frequencies calculated with DFT (Figs. S6 and S7), (iii) previous studies showing ring stretches of heteroatom-containing aromatics on Au electrodes [52–54], and (iv) the consistent, synchronous rise and fall of all four peak intensities relative to each other as a function of potential, suggesting that they belong to the same surface species. DFT frequencies show some coupling of ring and OCO modes (Fig. S7).

Spectra taken during voltammetry of furfural show similar features to those seen for FA, with the notable addition of a broad peak at 1381 cm^{-1}, which first appears during the forward sweep at 0.8 V. We propose this peak to relates to a reorientation of the furfural molecule to an “upright” configuration (ring plane perpendicular to surface), per the following reasons. The prominence, broadening, and onset potential of this peak were found to closely resemble a peak associated with furan, for which an ATR-SEIRAS voltammogram can be found in Fig. S3. The furan spectra can be interpreted through comparison with previous ATR studies of pyridine (another aromatic heterocycle), for which an ordered adlayer was found to bind to an Au electrode surface via the electronegative heteroatom (N in that case, O here). This orientation was potential dependent (confirmed using STM), and no ring oxidation products were observed over a similar range of potentials to those encountered in the present work [52]. It is therefore plausible that furan could undergo a similar process of surface self-assembly via the heteroatom, and by extension, the orientation of adsorbed furfural could also be impacted by potential. The assignment to an upright ordering of furfural is also consistent with ATR-SEIRAS selection rules, as the flat configuration of both the furan and furfural adsorbates are not expected to be visible. Further investiga-

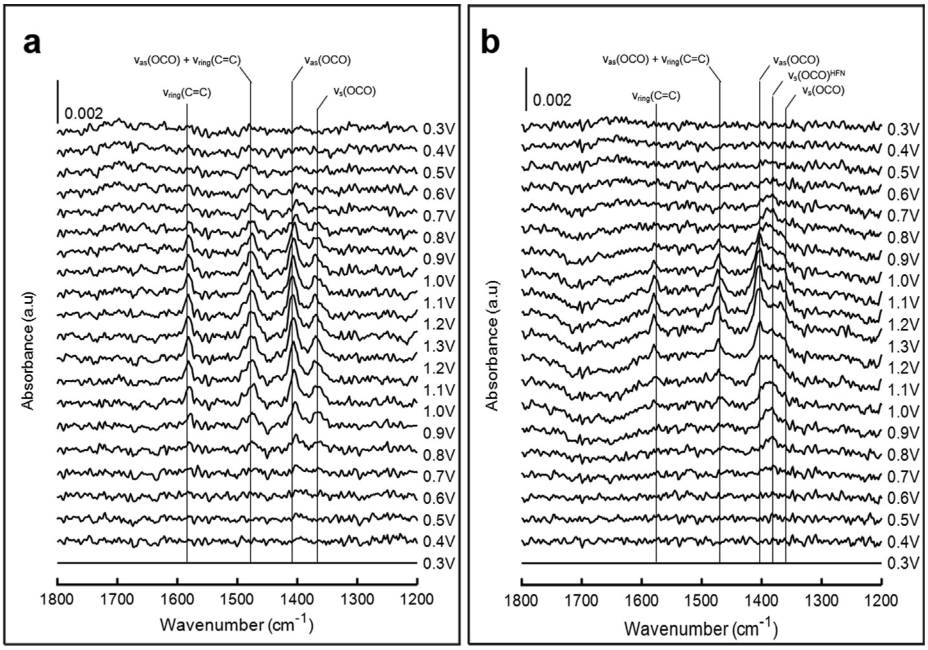

Fig. 4. ATR-SEIRAS difference spectra for the electro-oxidation of (a) 100 mM FA and (b) 100 mM furfural in 0.25 M $HClO_4$ on a Au film. Scan rate = 5 mV/s with the beginning of the CV corresponding to the bottom spectra of the figure.

tion via alternative techniques, e.g. in situ STM, would be valuable to provide more insight as to the exact nature of both furan and furfural orientation in this potential window. Despite the interpretation offered here, the conformation seen at 0.8 V could potentially also be attributed to (a) an intermediate in the pathway to FA formation, (b) a spectator species with higher resistance to oxidation (as is suspected to be the case for furan), or (c) possibly an intermediate in the pathway to HFN/MA. As potential increases to 1.0 V, this furfural-ring feature is overtaken by peaks associated with surface-bound furoate forming at 1373 cm^{-1} and 1412 cm^{-1}. The peak is slightly more persistent in the cathodic sweep, desorbing around 0.7 V, whereas the furoate desorption occurs around 0.8 V.

A proposed mechanism for the production of FA and resulting formation of an ordered, blocking layer of furoate is shown in Scheme 2. Furfural is initially oxidized to FA at potentials >0.8 V, and the resulting carboxylic acid is then primarily oxidized to a surface-bound carboxylate, with a small fraction undergoing desorption instead at potentials <1.2 V. This process continues until the furoate begins to form a high coverage layer blocking the Au surface, reducing the number of vacant sites available for reaction. At potentials <0.8 V, the furoate can be reversibly reduced back to FA, which will then be molecularly adsorbed and the equilibrium will favor desorption to solution-phase FA.

3.4. Density functional theory studies

To better understand the enhanced activity and selectivity to FA on Au relative to Pt, DFT calculations were used to compute elementary reaction energetics. Fig. 5 shows the reaction free energy diagram for conversion of furfural to FA on both Au(1 1 1) and Pt (1 1 1) electrodes at 1.0 V vs. the computational hydrogen electrode. Although solvation is not modeled, analyzing the difference in intermediate adsorption energies on Pt(1 1 1) and Au(1 1 1) surfaces should provide a reliable point of comparison due to the expected cancelation of errors in similar effects of surface solvation. FA desorption was found to be both unfavorable and likely to limit the reaction rate on both electrodes. However, desorption of FA from Au(1 1 1) is 1.08 eV more favorable than desorption from Pt(1 1 1), which may result in a higher proportion of available reac-

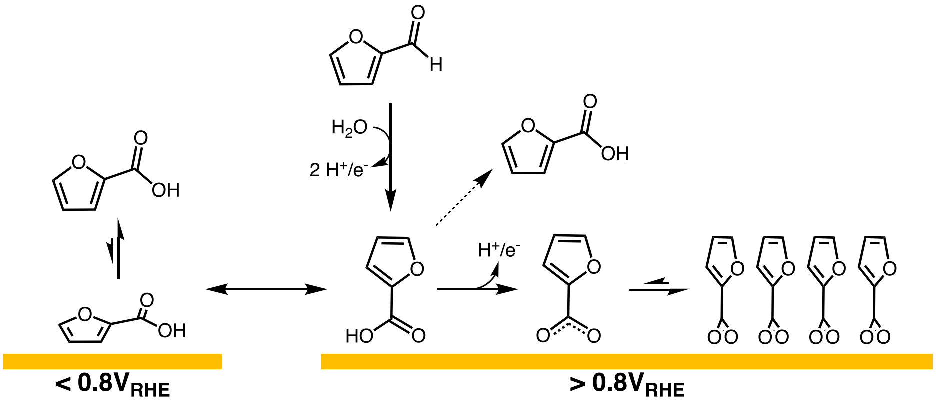

Scheme 2. Proposed mechanism of furfural electro-oxidation to furoic acid. At high potentials, strongly bond furoate forms an ordered monolayer and effectively blocks the Au surface.

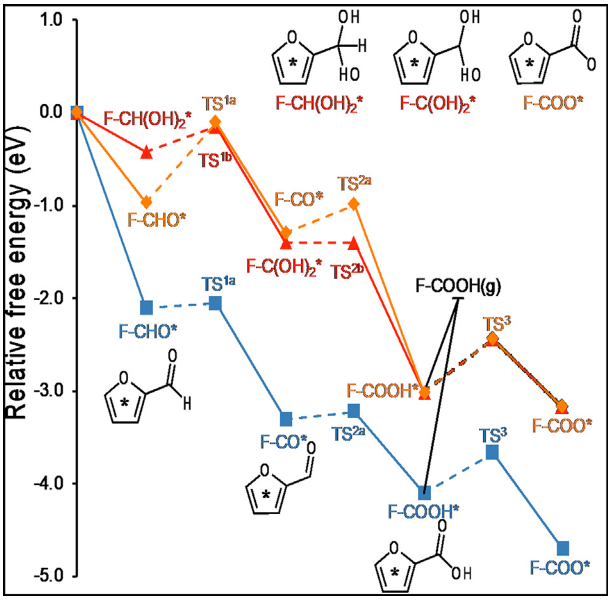

Fig. 5. Free energy diagram for furfural electrooxidation pathways on Au(1 1 1) [◆ - carbonyl route, ▲- diol route] and Pt(1 1 1) [■ - carbonyl route] at 1.0 V. Dashed lines indicate transition from the reactant state to the corresponding transition state.

tion sites on Au catalysts compared to Pt. This is in spite of the fact that the pathway to form FA on Pt is considerably more downhill, indicating that Pt may actually build up a blocking layer faster and more completely than Au. The challenge in providing quantitative accuracy of the desorption energy/barrier from a Au/aqueous interface makes it difficult, however, to be conclusive as to whether desorption would be the rate limiting step from the calculations alone.

Fig. 5 further includes the oxidation pathway of FA to surface bound furoate, which the ATR-SEIRAS experiments suggests should dominate at potentials >0.8 V and limit desorption of the FA product. Deeper oxidation of FA is expected to proceed through the furoate intermediate, and examination of its binding mode can provide insight into the likelihood and possible mechanism of proceeding to deeper oxidation products. In principle, the furoate can either bind parallel to the surface via π-interactions with the furyl ring (i.e. the “flat” orientation) or bind perpendicularly through the electronegative carboxylate (i.e. “upright” orientation), additionally stabilized by π-interactions between other adsorbed furoate species. The flat orientation is found to be the likely precursor to decarboxylation, as this mode orients the C—C bond between the pendant group and furyl ring near the surface, which is necessary for a surface-mediated dissociation step. The C—C dissociation barriers from the flat orientation are comparable on both Au(1 1 1) and Pt(1 1 1) (Fig. S11). However, relative energies between both conformations suggest a higher affinity for the flat orientation on Pt (0.97 eV more favorable) than on Au (0.17 eV more favorable), aligning well with experimental observation of higher C_4 production rates on Pt than Au.

Regarding the binding mode, it is noteworthy that the flat orientation on Au(1 1 1) does not show the extensive rehybridization of ring C atoms that is seen on Pt(1 1 1). If the D3 dispersion corrections are removed on the Au(1 1 1) surface, the upright orientation is energetically preferred by -0.12 eV. Given the presence of solvent interacting with both the surface and the adsorbate in the physical system, it is unclear whether the dispersion-corrected values are a more reliable representation of the relative preference of the flat versus upright binding modes. Consideration of higher coverage of furoate on the Au(1 1 1) surface (2 adsorbates per 3 × 3 unit cell) gave similar upright adsorption energies (Fig. S10), due to a competition between repulsive surface dipole–dipole interactions and attractive $\pi - \pi$ ring interactions among furoate adsorbates at increased coverage. However the higher coverage impeded formation of the flat orientation, suggesting higher furoate coverage may promote upright binding on Au(1 1 1); this orientation also can yield layers with larger total adsorption energy simply because higher coverage (more surface-oxygen bonds) can be achieved. Collectively, these DFT results suggest the higher affinity for the flat orientation facilitates the decarboxylation and subsequent deeper oxidations on Pt(1 1 1), whereas the Au surface is more likely to be “poisoned” by upright furoate and, therefore, unlikely to undergo decarboxylation and subsequent deeper oxidation steps.

Finally, Fig. 5 also shows the energetics of two plausible pathways for the activation of furfural on Au(1 1 1). The first pathway is similar to the route previously found to be preferable on Pt (1 1 1) [22]: activation of furfural occurs initially through the oxidative removal of the aldehyde hydrogen and is labelled as the “carbonyl route” in Fig. 5. An alternative path on Au(1 1 1) involves the initial solution-phase hydration of furfural to the geminal diol species (F-CH(OH)$_2$) with both species in equilibrium in acidic media [55]. This route is labelled the “diol route” in Fig. 5, where the gem-diol can subsequently undergo oxidative removal of the diol hydrogen. The diol route has a lower kinetic barrier (0.28 eV) for breaking the aldehyde C—H bond on Au compared to the corresponding C—H cleavage via the carbonyl route (0.86 eV). However, the transition state energies are similar for both C—H cleavage steps, leaving the dominant path dependent on the coverage regime, as well as the equilibrium between the initial reactants. The 2nd step in the carbonyl route requires the additional activation of water to OH_{ads} and has a barrier of 0.30 eV, while the 2nd step of the diol route (O—H cleavage) is barrierless. Based on the calculated energetics alone, the diol route is likely the more facile pathway to FA production on Au(1 1 1). A major caveat, however, is that gem-diol equilibrium is expected to skew heavily towards the aldehyde[54], thus limiting the amount of furfural available to go through this route. The diol route was also found to be facile on Pt(1 1 1) and, similar to the case on Au(1 1 1), was energetically comparable to the carbonyl route (Fig. S12). Regardless of reaction path on either catalyst, production of surface bound FA appears energetically facile at 1.0 V and is likely limited by product desorption.

3.5. Furoate inhibition studies

To experimentally test the hypothesis that either adsorbed FA or furoate suppresses furfural oxidation, voltammetric experiments were repeated in the presence of FA (Fig. 6). As seen earlier in Fig. 1, furfural alone in solution shifts the onset of Au oxidation to higher potentials as well as diminishes the corresponding reduction peak on the return sweep. However, the addition of just 1 mM FA to 100 mM furfural leads to further suppression of Au redox features and additionally diminishes the peaks associated with oxidation of the furfural molecule. This finding suggests that furoate does indeed strongly bind to the Au surface and is capable of blocking sites for furfural oxidation at low concentrations. The addition of 10 mM FA further hindered both oxidative processes, with the oxidation of furfural (Fig. 6 inset) almost completely shut down. This self-limiting behavior presents a challenge for running the reaction to high levels of conversion and suggests a need to explore approaches such as moderate elevation of temperature, continuous separation, or perhaps dynamic variation of the operating potential [56,57] in order to promote the desorption process. This must be balanced, however, with the fact that the self-assembly drives selectivity.

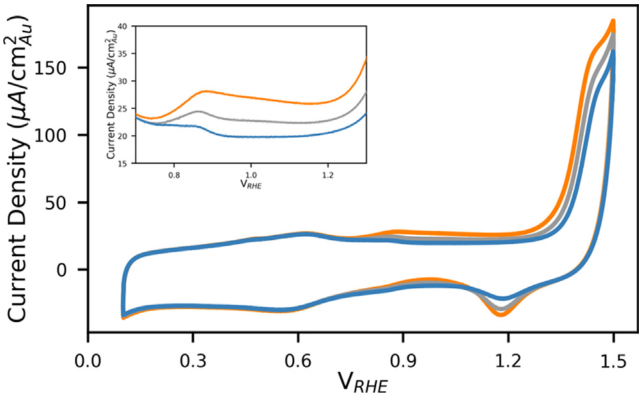

Fig. 6. Cyclic voltammograms for Au/C in 0.25 M $HClO_4$ with 100 mM (orange) furfural, 100 mM furfural + 1 mM FA (grey), and 100 mM furfural + 10 mM FA (blue) present. Scan rate = 20 mV/s.

4. Conclusions

In summary, Au/C was investigated as a catalyst for the electro-oxidation of furfural in acidic aqueous electrolyte. Voltammetry experiments showed the onset of an initial oxidation process at ~0.8 V followed by the light-off of a secondary process at 1.2 V, coinciding with the oxidation potential of Au. A flow reactor was used to perform steady-state oxidation experiments and showed FA to be the major product, with higher activity and F.E. than seen previously in studies on Pt/C. Varying the initial concentration of furfural showed higher selectivity to decarboxylation products at low concentrations (10 mM), but consistent high selectivity to FA at higher concentrations (50 and 100 mM), suggesting that a surface coverage approaching saturation plays a role in the formation of FA. ATR-SEIRAS experiments provided evidence supporting this hypothesis and showed that the adsorption of FA is potential-dependent and is initiated by the reversible oxidation of FA to furoate at ~0.8 V. Experiments examining furfural and furan oxidation on Au showed the presence of a species which may be a spectator, an altered adsorption mode of furfural, or an intermediate in the formation of deeper oxidation products at >1.2 V. However, the most abundant surface species formed during furfural oxidation is the resulting furoate, which binds in a bidentate conformation and eventually blocks the Au surface, limiting the net oxidation rate. DFT calculations showed downhill electro-oxidation energetics on Au(111) and Pt(111), suggesting the formation of FA is facile at potentials where oxidation is experimentally observed for both catalysts; the calculations also corroborated vibrational assignments. Finally, voltammetry experiments confirmed that the introduction of small amounts of FA (1–10 mM) greatly inhibited the oxidation of furfural. Apart from the previously discussed opportunities to increase conversion via changes to operating conditions (temperature, modulated potential, separation schemes), future work targeting alloys with characteristics that impede carboxylic acid poisoning or C—C bond cleavage should be pursued. In particular, designing for surface ensembles that break up furoate self-assembly while also hindering adsorption in flat-lying conformations that lead to C_4 products would be a valuable next step.

Declaration of Competing Interest

The authors declare that they have no known competing financial interests or personal relationships that could have appeared to influence the work reported in this paper.

Acknowledgements

A.M.R. acknowledges support from the NSF Graduate Research Fellowship (#1144083). The authors acknowledge support from the National Science Foundation (CHE-1665176, CHE-1665155). This work used the Extreme Science and Engineering Discovery Environment (XSEDE), which is supported by National Science Foundation grant number ACI-1053575. N.A. acknowledges training provided by the Computational Materials Education and Training (CoMET) NSF Research Traineeship (DGE-1449785).

Appendix A. Supplementary material

Supplementary data to this article can be found online at https://doi.org/10.1016/j.jcat.2020.08.034.

References

[1] A. Banerjee, G.R. Dick, T. Yoshino, M.W. Kanan, Carbon dioxide utilization via carbonate-promoted C-H carboxylation, Nature 531 (2016) 215–219, https://doi.org/10.1038/nature17185.
[2] G. Shen, S. Zhang, Y. Lei, Z. Chen, G. Yin, Synthesis of 2,5-furandicarboxylic acid by catalytic carbonylation of renewable furfural derived 5-bromofuroic acid, Mol. Catal. 455 (2018) 204–209, https://doi.org/10.1016/j.mcat.2018.06.015.
[3] K.A.P. Payne, S.A. Marshall, K. Fisher, M.J. Cliff, D.M. Cannas, C. Yan, et al., Enzymatic carboxylation of 2-furoic acid yields 2,5- furandicarboxylic acid (FDCA), ACS Catal. 9 (2019) 2854–2865, https://doi.org/10.1021/acscatal.8b04862.
[4] G.R. Dick, A.D. Frankhouser, A. Banerjee, M.W. Kanan, A scalable carboxylation route to furan-2,5-dicarboxylic acid, Green Chem. 19 (2017) 2966–2972, https://doi.org/10.1039/C7GC01059A.
[5] S. Zhang, J. Lan, Z. Chen, G. Yin, G. Li, Catalytic synthesis of 2,5-furandicarboxylic acid from furoic acid: transformation from C5 platform to C6 derivatives in biomass utilizations, ACS Sustain. Chem. Eng. 5 (2017) 9360–9369, https://doi.org/10.1021/acssuschemeng.7b02396.
[6] R. Mariscal, P. Maireles-Torres, M. Ojeda, I. Sádaba, M. López Granados, Furfural: a renewable and versatile platform molecule for the synthesis of chemicals and fuels, Energy Environ. Sci. 9 (2016) 1144–1189, https://doi.org/10.1039/C5EE02666K.
[7] X. Li, P. Jia, T. Wang, Furfural: a promising platform compound for sustainable production of C4 and C5 chemicals, ACS Catal. 6 (2016) 7621–7640, https://doi.org/10.1021/acscatal.6b01838.
[8] P. Verdeguer, N. Merat, A. Gaset, Lead/platinum on charcoal as catalyst for oxidation of furfural. Effect of main parameters, Appl. Catal. A 112 (1994) 1–11, https://doi.org/10.1016/0926-860x(94)80133-9.
[9] M. Douthwaite, X. Huang, S. Iqbal, P.J. Miedziak, G.L. Brett, S.A. Kondrat, et al., The controlled catalytic oxidation of furfural to furoic acid using AuPd/Mg(OH)2, Catal. Sci. Technol. 7 (2017) 5284–5293, https://doi.org/10.1039/C7CY01025G.
[10] N.K. Gupta, A. Fukuoka, K. Nakajima, Metal-free and selective oxidation of furfural to furoic acid with an N-heterocyclic carbene catalyst, ACS Sustain. Chem. Eng. 6 (2018) 3434–3442, https://doi.org/10.1021/acssuschemeng.7b03681.
[11] L.A. Badovskaya, L.V. Povarova, Oxidation of furans (Review), Chem. Heterocycl. Compd. 45 (2009) 1023–1034, https://doi.org/10.1007/s10593-009-0390-8.
[12] Y. Kwon, K.J.P. Schouten, J.C. van der Waal, E. de Jong, M.T.M. Koper, Electrocatalytic conversion of furanic compounds, ACS Catal. 6 (2016) 6704–6717, https://doi.org/10.1021/acscatal.6b01861.
[13] K. Li, Y. Sun, Electrocatalytic upgrading of biomass-derived intermediate compounds to value-added products, Chem. Eur. J. 24 (2018) 18258–18270, https://doi.org/10.1002/chem.201803319.
[14] N. Jiang, X. Liu, J. Dong, B. You, X. Liu, Y. Sun, Electrocatalysis of furfural oxidation coupled with H2 evolution via nickel-based electrocatalysts in water, ChemNanoMat 3 (2017) 491–495, https://doi.org/10.1002/cnma.201700076.
[15] L. Du, Y. Shao, J. Sun, G. Yin, C. Du, Y. Wang, Electrocatalytic valorisation of biomass derived chemicals, Catal. Sci. Technol. 8 (2018) 3216–3232, https://doi.org/10.1039/C8CY00533H.
[16] H.G. Cha, K.-S. Choi, Combined biomass valorization and hydrogen production in a photoelectrochemical cell, Nat. Chem. 7 (2015) 328–333, https://doi.org/10.1038/nchem.2194.
[17] G. Chamoulaud, D. Floner, C. Moinet, C. Lamy, E.M. Belgsir, Biomass conversion II: simultaneous electrosyntheses of furoic acid and furfuryl alcohol on modified graphite felt electrodes, Electrochim. Acta 46 (2001) 2757–2760.
[18] S. Jung, E.J. Biddinger, Controlling competitive side reactions in the electrochemical upgrading of furfural to biofuel, Energy Technol. 6 (2018) 1370–1379, https://doi.org/10.1002/ente.201800216.

[19] N. Shan, M.K. Hanchett, B. Liu, Mechanistic insights evaluating Ag, Pb, and Ni as electrocatalysts for furfural reduction from first-principles methods, J. Phys. Chem. C 121 (2017) 25768–25777, https://doi.org/10.1021/acs.jpcc.7b06778.

[20] X.H. Chadderdon, D.J. Chadderdon, J.E. Matthiesen, Y. Qiu, J.M. Carraher, J.-P. Tessonnier, et al., Mechanisms of furfural reduction on metal electrodes: distinguishing pathways for selective hydrogenation of bioderived oxygenates, J. Am. Chem. Soc. 139 (2017) 14120–14128, https://doi.org/10.1021/jacs.7b06331.

[21] A.M. Román, J.C. Hasse, J.W. Medlin, A. Holewinski, Elucidating acidic electro-oxidation pathways of furfural on platinum, ACS Catal. 9 (2019) 10305–10316, https://doi.org/10.1021/acscatal.9b02656.

[22] L. Gong, N. Agrawal, A. Roman, A. Holewinski, M.J. Janik, Density functional theory study of furfural electrochemical oxidation on the Pt (1 1 1) surface, J. Catal. 373 (2019) 322–335, https://doi.org/10.1016/j.jcat.2019.04.012.

[23] C.P. Ferraz, A.G.M.D. Silva, T.S. Rodrigues, P.H.C. Camargo, S. Paul, R. Wojcieszak, Furfural oxidation on gold supported on MnO2: influence of the support structure on the catalytic performances, Appl. Sci. 8 (2018) 1246, https://doi.org/10.3390/app8081246.

[24] A. Roselli, Y. Carvalho, F. Dumeignil, F. Cavani, S. Paul, R. Wojcieszak, Liquid phase furfural oxidation under uncontrolled pH in batch and flow conditions: the role of in situ formed base, Catalysts 10 (2020) 1–12, https://doi.org/10.3390/catal10010073.

[25] S.E. Davis, B.N. Zope, R.J. Davis, On the mechanism of selective oxidation of 5-hydroxymethylfurfural to 2,5-furandicarboxylic acid over supported Pt and Au catalysts, Green Chem. 14 (2012) 143–147, https://doi.org/10.1039/C1GC16074E.

[26] D.J. Chadderdon, J. Le Xin, Y. Qi, P. Qiu, K.L.M. Krishna, et al., Electrocatalytic oxidation of 5-hydroxymethylfurfural to 2,5-furandicarboxylic acid on supported Au and Pd bimetallic nanoparticles, Green Chem. 16 (2014) 3778–3786, https://doi.org/10.1039/C4GC00401A.

[27] P. Parpot, A.P. Bettencourt, G. Chamoulaud, K.B. Kokoh, E.M. Belgsir, Electrochemical investigations of the oxidation–reduction of furfural in aqueous medium, Electrochim. Acta 49 (2004) 397–403, https://doi.org/10.1016/j.electacta.2003.08.021.

[28] S.R. Kubota, K.-S. Choi, Electrochemical valorization of furfural to maleic acid, ACS Sustain. Chem. Eng. 6 (2018) 9596–9600, https://doi.org/10.1021/acssuschemeng.8b02698.

[29] H. Wu, J. Song, H. Liu, Z. Xie, C. Xie, Y. Hu, et al., An electrocatalytic route for transformation of biomass-derived furfural into 5-hydroxy-2(5 H)-furanone, Chem. Sci. 8 (2019) 16104–16107, https://doi.org/10.1039/C9SC00322C.

[30] C. Dai, L. Sun, H. Liao, B. Khezri, R.D. Webster, A.C. Fisher, et al., Electrochemical production of lactic acid from glycerol oxidation catalyzed by AuPt nanoparticles, J. Catal. 356 (2017) 14–21, https://doi.org/10.1016/j.jcat.2017.10.010.

[31] H. Miyake, S. Ye, M. Osawa, Electroless deposition of gold thin films on silicon for surface-enhanced infrared spectroelectrochemistry, Electrochem. Commun. 4 (2002) 973–977, https://doi.org/10.1016/S1388-2481(02)00510-6.

[32] P.E. Blöchl, Projector augmented-wave method, Phys. Rev. B. 50 (1994) 17953–17979, https://doi.org/10.1103/PhysRevB.50.17953.

[33] G. Kresse, D. Joubert, From ultrasoft pseudopotentials to the projector augmented-wave method, Phys. Rev. B. 59 (1999) 1758–1775, https://doi.org/10.1103/PhysRevB.59.1758.

[34] J.P. Perdew, J.A. Chevary, S.H. Vosko, K.A. Jackson, M.R. Pederson, D.J. Singh, et al., Atoms, molecules, solids, and surfaces: Applications of the generalized gradient approximation for exchange and correlation, Phys. Rev. B. 46 (1992) 6671, https://doi.org/10.1103/PhysRevB.46.6671.

[35] A. Gulans, M.J. Puska, R.M. Nieminen, Linear-scaling self-consistent implementation of the van der Waals density functional, Phys. Rev. B. 79 (2009), https://doi.org/10.1103/PhysRevB.79.201105 201105.

[36] G. Kresse, J. Furthmüller, Efficiency of ab-initio total energy calculations for metals and semiconductors using a plane-wave basis set, Comput. Mater. Sci. 6 (1996) 15–50.

[37] G. Kresse, J. Furthmüller, Efficient iterative schemes for *ab initio* total-energy calculations using a plane-wave basis set, Phys. Rev. B. 54 (1996) 11169–11186, https://doi.org/10.1103/PhysRevB.54.11169.

[38] L.O. Mark, N. Agrawal, A.M. Román, A. Holewinski, M.J. Janik, J.W. Medlin, Insight into the oxidation mechanism of furanic compounds on Pt(111), ACS Catal. 9 (2019) 11360–11370, https://doi.org/10.1021/acscatal.9b03983.

[39] G. Henkelman, B.P. Uberuaga, H. Jónsson, A climbing image nudged elastic band method for finding saddle points and minimum energy paths, J. Chem. Phys. 113 (2000) 9901–9904, https://doi.org/10.1063/1.1329672.

[40] D. McQuarrie, Statistical Mechanics, University Science Books, Sausalito, CA, 2000.

[41] G. Rostamikia, A.J. Mendoza, M.A. Hickner, M.J. Janik, First-principles based microkinetic modeling of borohydride oxidation on a Au(1 1 1) electrode, J. Power Sources 196 (2011) 9228–9237, https://doi.org/10.1016/j.jpowsour.2011.07.042.

[42] I. Merino-Jimenez, M.J. Janik, C. Ponce de Leon, F.C. Walsh, Pd–Ir alloy as an anode material for borohydride oxidation, J. Power Sources 269 (2014) 498–508, https://doi.org/10.1016/j.jpowsour.2014.06.140.

[43] X. Nie, W. Luo, M.J. Janik, A. Asthagiri, Reaction mechanisms of CO2 electrochemical reduction on Cu(111) determined with density functional theory, J. Catal. 312 (2014) 108–122, https://doi.org/10.1016/j.jcat.2014.01.013.

[44] A.J. Bard, L.R. Faulkner, Electrochemical Methods, second ed., John Wiley & Sons, 2001.

[45] A.M. Román, J. Dudoff, A. Baz, A. Holewinski, Identifying "Optimal" electrocatalysts: impact of operating potential and charge transfer model, ACS Catal. 7 (2017) 8641–8652, https://doi.org/10.1021/acscatal.7b03235.

[46] S.H. Pang, A.M. Román, J.W. Medlin, Adsorption orientation-induced selectivity control of reactions of benzyl alcohol on Pd(111), J. Phys. Chem. C 116 (2012) 13654–13660, https://doi.org/10.1021/jp303147c.

[47] R.M. Williams, S.H. Pang, J.W. Medlin, Ring-opening and oxidation pathways of furanic oxygenates on oxygen-precovered Pd(111), J. Phys. Chem. C 118 (2014) 27933–27943, https://doi.org/10.1021/jp509284d.

[48] L.O. Mark, A.H. Jenkins, H. Heinz, J.W. Medlin, Furfuryl alcohol deoxygenation, decarbonylation, and ring-opening on Pt(111), Surf. Sci. 677 (2018) 333–340, https://doi.org/10.1016/j.susc.2018.07.001.

[49] H.-Q. Li, S.G. Roscoe, J. Lipkowski, FTIR studies of benzoate adsorption on the Au (111) electrode, J. Electroanal. Chem. (1999) 67–75, https://doi.org/10.1016/S0022-0728(99)00413-1.

[50] W.-K. Paik, S. Han, W. Shin, Y. Kim, Adsorption of carboxylic acids on gold by anodic reaction, Langmuir 19 (2003) 4211–4216, https://doi.org/10.1021/la026836s.

[51] B. Han, Z. Li, T. Wandlowski, Adsorption and self-assembly of aromatic carboxylic acids on Au/electrolyte interfaces, Anal. Bioanal. Chem. 388 (2007) 121–129, https://doi.org/10.1007/s00216-007-1166-6.

[52] Wen-Bin Cai, Li-Jun Wan, Hiroyuki Noda, Yuichi Hibino, A. Kenichi Ataka, M. Osawa, Orientational phase transition in a pyridine adlayer on gold(111) in aqueous solution studied by in situ infrared spectroscopy and scanning tunneling microscopy, Langmuir (1998), https://doi.org/10.1021/la980617i.

[53] T. Wandlowski, K. Ataka, D. Mayer, In situ infrared study of 4,4'-bipyridine adsorption on thin gold films, Langmuir 18 (2002) 4331–4341, https://doi.org/10.1021/la025585k.

[54] A.C. Chen, D.F. Yang, J. Lipkowski, S.G. Sun, B. Pettinger, In situ FTIR studies of 4-cyanopyridine adsorption at the Au(111) electrode, Can. J. Chem. (2011), https://doi.org/10.1139/v96-259.

[55] L.A. Badovskaya, V.V. Poskonin, Metal nature effect on catalytic reactions in furfural-H2O2-H2O-group V or VI d-metal salt systems in acid media, Kinet. Catal. 56 (2015) 164–172, https://doi.org/10.1134/S0023158415020019.

[56] J. Gopeesingh, M.A. Ardagh, M. Shetty, S. Burke, P.J. Dauenhauer, O.A. Abdelrahman, Resonance-promoted formic acid oxidation via dynamic electrocatalytic modulation, ChemRxiv. (2020), https://doi.org/10.26434/chemrxiv.11972031.v1.

[57] D.E. Blanco, B. Lee, M.A. Modestino, Optimizing organic electrosynthesis through controlled voltage dosing and artificial intelligence, PNAS 116 (2019) 17683–17689, https://doi.org/10.1073/pnas.1909985116.